

PAPER

Intermediate- k density and magnetic field fluctuations during inter-ELM pedestal evolution in MAST

To cite this article: J C Hillesheim *et al* 2016 *Plasma Phys. Control. Fusion* **58** 014020

View the [article online](#) for updates and enhancements.

Related content

- [Doppler backscattering for spherical tokamaks and measurement of high- \$k\$ density fluctuation wavenumber spectrum in MAST](#)
J.C. Hillesheim, N.A. Crocker, W.A. Peebles *et al.*
- [Improved understanding of physics processes in pedestal structure, leading to improved predictive capability for ITER](#)
R.J. Groebner, C.S. Chang, J.W. Hughes *et al.*
- [Quasi-coherent fluctuations limiting the pedestal growth on Alcator C-Mod: experiment and modelling](#)
A. Diallo, J.W. Hughes, S-G. Baek *et al.*

Recent citations

- [Pedestal evolution physics in low triangularity JET tokamak discharges with ITER-like wall](#)
C. Bowman *et al*
- [Collisionality scaling of the electron heat flux in ETG turbulence](#)
G J Colyer *et al*
- [Ion-scale turbulence in MAST: anomalous transport, subcritical transitions, and comparison to BES measurements](#)
F van Wyk *et al*

Intermediate- k density and magnetic field fluctuations during inter-ELM pedestal evolution in MAST

J C Hillesheim¹, D Dickinson², C M Roach¹, S Saarelma¹, R Scannell¹,
A Kirk¹, N A Crocker³, W A Peebles³, H Meyer¹ and the MAST Team¹

¹ CCFE, Culham Science Centre, Abingdon, Oxon OX14 3DB, UK

² York Plasma Institute, Department of Physics, University of York, Heslington, York YO10 5DD, UK

³ University of California, Los Angeles, Los Angeles, California 90095-7099, USA

E-mail: jon.hillesheim@ccfe.ac.uk

Received 19 June 2015, revised 7 September 2015

Accepted for publication 11 September 2015

Published 3 November 2015



Abstract

Measurements of local density and magnetic field fluctuations near the pedestal top, conditionally averaged over the edge localized mode (ELM) cycle, have been made in Mega Amp Spherical Tokamak (MAST). A Doppler backscattering (DBS) system installed at MAST was used to measure intermediate- k ($k_{\perp}\rho_i \approx 3$ to 4) density fluctuations at the top of the pedestal. A novel diagnostic technique combining DBS with cross-polarization scattering (CP-DBS) enabled magnetic field fluctuations to also be locally measured at similar wave numbers. Polarization isolation and other effects for CP-DBS are discussed. Both measurements were used in a series of high- β ($\beta_n \approx 4.0$ – 4.5) MAST plasmas with large type-I ELMs with an ~ 8 to 9 ms period where microtearing modes (MTMs) had been predicted to be unstable in similar conditions (Dickinson 2012 *Phys. Rev. Lett.* **108** 135002). The measured density fluctuation level increased by a factor of about 4 between 2 and 4 ms after the ELM, which was correlated with the recovery of the density profile while the temperature pedestal height continued to increase slowly. Magnetic field fluctuations showed different temporal behaviors, slowly increasing throughout the ELM cycle as the local β increased. Linear GS2 calculations show both MTM and electron temperature gradient (ETG) modes unstable at similar wave numbers as the measurements (although with more overlap between ETG wave numbers and diagnostic spectral resolution) at the top of the pedestal, along with kinetic ballooning modes are unstable lower in the pedestal (at larger wavelengths). The inferred ratio of fluctuation levels from experiment was $(\delta B/B)/(\delta n/n) \approx 1/20$. The comparable ratios from GS2 were $(\delta B/B)/(\delta n/n) \approx 0.4$ for the MTM and $(\delta B/B)/(\delta n/n) \approx 0.02$ for the ETG. Both the experimental wave number range and the fluctuation ratio are more similar to the linear characteristics of the ETG than the MTM. These results imply that intermediate- k fluctuations due to the ETG play a role in inter-ELM pedestal evolution.

Keywords: cross-polarization scattering, diagnostics, Doppler backscattering, pedestal, turbulence

(Some figures may appear in colour only in the online journal)

1. Introduction

In tokamaks operating in the H-mode, an edge transport barrier forms. This significantly increases the global energy

confinement time and increases the achievable central temperature by forming a region at the edge of the plasma with a large pressure gradient, which is called the pedestal. The underlying physics of the pedestal is crucial for extrapolating

the operation of current tokamak devices to future experiments. Intermittent instabilities called edge localized modes (ELMs) cause the pedestal to collapse, resulting in a cycle of crashes and recoveries. In the widely used EPED model [1] the kinetic ballooning mode (KBM) and peeling-ballooning constraints are included to predict the pedestal pressure height and width at the onset of an ELM. However, experiments observe the evolution of the temperature and density profiles during the inter-ELM period [2, 3], which requires a more sophisticated model than is needed to only predict the end point of the ELM cycle. For recent reviews of ELM physics, see [4, 5]. The inter-ELM evolution of the temperature and density profiles is important for advancing the physics basis of ELM control—such as with applied 3D fields, vertical kicks, or pellets—where the goal is to interfere with the natural ELM cycle and prevent or modify the onset of ELMs. It has also been demonstrated that by navigating the stable regions of peeling-ballooning space, it is possible to access high performance regimes [6]. Understanding the evolution of the pedestal between ELMs requires understanding the relevant physical mechanisms, both sources and transport. In this article we investigate the influence of intermediate scale instabilities $k_{\perp}\rho_i \approx 3$ to 4 (where k_{\perp} is the binormal wave number and ρ_i is the ion gyroradius) between ELMs in the Mega Amp Spherical Tokamak (MAST) [7].

In the context of models like EPED, kinetic ballooning modes are predicted to set the pedestal pressure gradient. Long wavelength fluctuations, $k_{\perp}\rho_i \sim 0.1$, consistent with the kinetic ballooning mode have been identified in DIII-D [8, 9] and Alcator C-mod [10, 11]. The impact of smaller scale instabilities in the pedestal has also been investigated. Microtearing modes (MTMs) [12, 13] have been predicted to be unstable at the top of the H-mode pedestal in MAST [14, 15], playing a role in determining pedestal transport between ELMs and therefore of pedestal structure and ELM stability. MTMs have also been found to be unstable in simulations at the top of JET H-mode pedestals [16] and have been found to be consistent with velocimetry analysis of temperature fluctuations near the top of the pedestal in AUG [17]. Comparison of the scaling of turbulence characteristics also found low- k pedestal fluctuations to be consistent with MTM (although not consistent solely with MTM) in the National Spherical Torus Experiment (NSTX) [18]. The higher wave number electron temperature gradient (ETG) modes also have long been conjectured to be important since they have higher growth rates and are harder to suppress with $E \times B$ shear [19]. More recent analysis of transport in the pedestal and gyrokinetic simulations also have found the ETG to play a significant role [20, 21]. Both MTM and ETG also have been found to be unstable in the linear stability analysis of NSTX [22].

We present a novel diagnostic technique, combining Doppler backscattering (DBS) and cross-polarization scattering. This has enabled measurements sensitive to local internal magnetic field fluctuations at the radial location where MTMs have been predicted to be unstable in MAST. Subsequent linear gyrokinetic analysis of the discharges where measurements were acquired found both MTMs and ETG unstable at the top of the pedestal. There was a larger

overlap in diagnostic wave number sensitivity with wave numbers where the ETG was the fastest growing linear mode than with MTM. The experimentally inferred ratio between magnetic field and density fluctuations also was closer to the ETG than the MTM by an order of magnitude.

DBS (also called Doppler reflectometry) is a refraction localized scattering technique [23], which is typically used to measure intermediate and high wave number ($k_{\perp}\rho_i > 1$) density fluctuations and their laboratory frame propagation velocity. Two eight-channel DBS systems and a quasioptical system with 2D steering and a rotatable polarizer were installed at MAST [24]. The two systems were combined with a polarizer such that either both systems could be operated monostatically (launch and receive radiation with the same antenna) at the same time with orthogonal polarizations for each system, or one system could be operated bistatically (launch and receive with different antennas), launching and receiving orthogonal polarizations.

Cross-polarization scattering has been theoretically investigated [25, 26], and results have been reported from several experiments [27–30]. In principle, collective scattering diagnostics are sensitive to index of refraction fluctuations, which could be due to either density fluctuations or magnetic field fluctuations. The fundamental idea is that density fluctuations preserve the polarization of the incident wave, while magnetic field fluctuations rotate the polarization by 90° due to the scattered electric field arising from the vector product of the incident electric field and the fluctuating magnetic field $\mathbf{E}_s \sim \mathbf{E}_i \times (\delta\mathbf{B})/B$. Cross-polarization scattering has historically been challenging since $\delta B/B \ll \delta n/n$ so that small polarization mismatches, spurious detected light (e.g., reflections from a far wall), or other polarization transforming effects can easily contaminate the measurement.

In section 2, we discuss the cross-polarization Doppler backscattering (CP-DBS) technique, including numerous effects that could potentially contaminate the measurement. Section 3 presents experimental results, including ELM cycle conditionally averaged electron density and temperature profiles along with ELM cycle conditionally averaged DBS and CP-DBS measurements. Linear gyrokinetic analysis from the code GS2 can be found in section 4. Finally, a discussion of the results and a conclusions are in section 5.

2. Considerations for cross-polarization scattering

Although there have been several attempts to implement cross-polarization scattering over the past 20 years [27–30], it has not become a routine diagnostic. In this section we discuss several effects that can contaminate the cross-polarization signal and assess their impact for our measurements.

2.1. Assessing polarization match

A challenging experimental aspect of cross-polarization scattering measurements is matching the launched polarization to the plasma magnetic field pitch angle. If this is not done correctly, the impact is the leading order effect on the

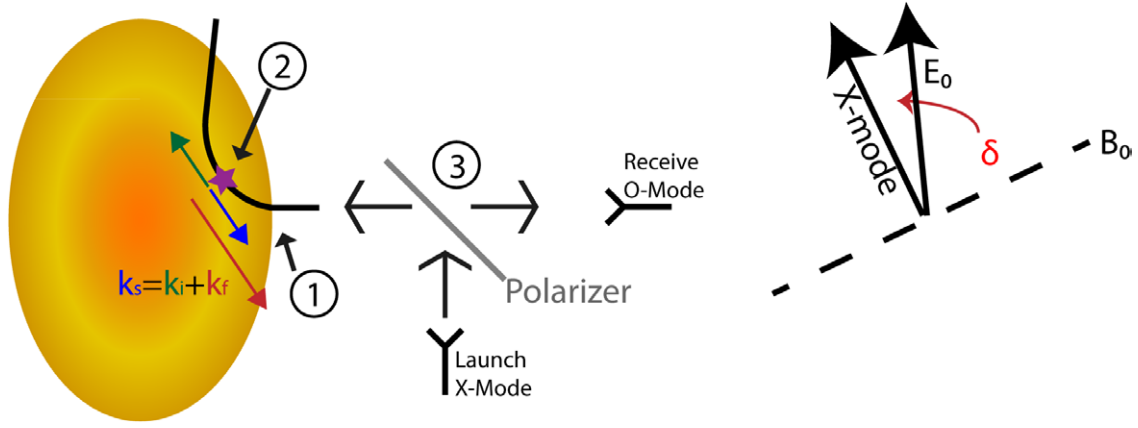


Figure 1. Schematic of CP-DBS, showing locations where polarization-dependent effects occur: (1) Polarization mismatch between launched wave and magnetic field at edge of plasma, (2) scattering from different fields into different polarizations, and (3) rejection of unwanted polarization via rotatable polarizer. On the right, the polarization mismatch angle is noted as δ .

measurement. Regardless of the cause of the polarization mismatch, we present a simple argument that it is possible to bound the level of polarization matching from the data themselves.

Figure 1 shows a schematic of the diagnostic setup for CP-DBS; further details in [24]. The vector relation among the incident, scattered, and fluctuating wave vectors are annotated and discussed further in section 2.2. An advantage of this scheme, by using two passes through the same polarizer, is that the launched and detected polarizations are guaranteed to be orthogonal. In MAST the beam is first launched vertically from the V-band scalar horn with a 45° twist to reduce lost power transmitted through the polarizer. X-mode polarization was launched for O-mode reception. The rotatable polarizer is set at a best estimate to minimize δ , which is the angle between the electric field vector of the launched beam and the linear polarization that couples best to the X-mode in the plasma. Transmitted power travels to the ceiling, $10 +$ m distance and is assumed lost. At point (1) in figure 1, there is, in general, an initial polarization mismatch, splitting the relative launched power into orthogonal polarizations schematically:

$$P_X \rightarrow \cos^2 \delta, \quad (1)$$

$$P_O \rightarrow \sin^2 \delta. \quad (2)$$

The scattering occurs at (2), localized in the usual way for DBS. The four possibilities are now

$$S_{X \rightarrow O} \cos^2 \delta, \quad (3)$$

$$S_{X \rightarrow X} \cos^2 \delta, \quad (4)$$

$$S_{O \rightarrow O} \sin^2 \delta, \quad (5)$$

$$S_{O \rightarrow X} \sin^2 \delta, \quad (6)$$

where $S_{i \rightarrow j}$ is

$$S_{i \rightarrow j} = \chi_{i \rightarrow j} \frac{\tilde{f}^2}{f^2}. \quad (7)$$

$\chi_{i \rightarrow j}$ is the inherent efficiency of the scattering process, where i is the initial polarization, j is the resultant polarization, and f is either n_e or B . The $\chi_{i \rightarrow j}$ are, in principle, calculable via the Born approximation for small amplitude scattering when the polarizations are separable [26], with the caveat that those calculations do not include the effect of refraction on the beam, which is fundamental to the DBS technique. Scattering efficiency calculations have been performed for standard DBS [31] but not for cross-polarization scattering. We also are assuming that we can treat X-mode and O-mode propagation independently and that they are not coupled by the non-Wentzel–Kramers–Brillouin (non-WKB) effects (i.e., there is no spatial scale separation between the density gradient and the wave), discussed further below. In general, all the $\chi_{i \rightarrow j}$'s are predicted to be of the same order of magnitude, which also is consistent with full wave modeling [32]. Conversely, the ratio of fluctuation levels is likely a large effect with estimates for $(\tilde{B}/B)^2/(\tilde{n}/n)^2 \sim 10^{-2} - 10^{-5}$.

We then have the backscattered signals that are transmitted through the rejecting polarizer. For perfect alignment only $P_{B,O}$ is nonzero.

$$P_{B,O} = S_{X \rightarrow O} \cos^4 \delta, \quad (8)$$

$$P_{n,X} = S_{X \rightarrow X} \cos^2 \delta \sin^2 \delta, \quad (9)$$

$$P_{n,O} = S_{O \rightarrow O} \sin^2 \delta \cos^2 \delta, \quad (10)$$

$$P_{B,X} = S_{O \rightarrow X} \sin^4 \delta. \quad (11)$$

The received power contributions are $P_{f,i}$, where f is the field inducing the scattering and i is the received polarization. $P_{B,X}$ can be ignored since it should mostly be absorbed at the upper hybrid resonance and would in any case be small due to the factor of $\sin^4 \delta$. $P_{B,O}$ is the signal of interest. There is a second rejection at the horn, which is at a 45° angle; however, this affects all contributions equally.

The issue is that, although δ should be small, the ratio $(\tilde{B}/B)^2/(\tilde{n}/n)^2$ could be small enough to compensate and complicate the interpretation of measurements. Since the $S_{i \rightarrow j}$'s are predominantly determined by the ratio of fluctuation levels,

which are unknown, we wish to find any empirical means to estimate contributions to the measured signal. DBS has the advantage that the scattering locations from the X-mode and O-mode cutoffs are spatially separated and therefore if there is significant misalignment, there should be two concurrent DBS peaks. We therefore have the measurable empirical ratio R_1 between the powers in the two peaks (assuming the E_r profile is such that they are separable)

$$R_1 = \frac{P_{B,O} + P_{n,X}}{P_{n,O}} = \frac{S_{X \rightarrow O} \cos^2 \delta + S_{X \rightarrow X} \sin^2 \delta}{S_{O \rightarrow O} \sin^2 \delta}. \quad (12)$$

The ratio of interest, R_2 , is the ratio of power originating at the X-mode cutoff from scattering by magnetic field fluctuations to scattering by density fluctuations,

$$R_2 = \frac{P_{B,O}}{P_{n,X}} = \frac{S_{X \rightarrow O}}{S_{X \rightarrow X}} \frac{1}{\tan^2 \delta}. \quad (13)$$

The relation between the ratios is

$$R_2 = \frac{S_{O \rightarrow O}}{S_{X \rightarrow X}} R_1 - 1. \quad (14)$$

$S_{O \rightarrow O}/S_{X \rightarrow X} \sim 1$ since the density fluctuation levels should not be greatly different (for the same launched frequency and trajectory, the wave number should be similar), therefore if $R_1 \gg 1$ (i.e., a single Doppler peak is present) then R_2 is large (i.e., magnetic field fluctuations dominate the measurement). Note this is independent of the actual ratio of fluctuation levels. This means that if the misalignment is large enough that signals from the X-mode cutoff due to both density and magnetic field fluctuations are received, then that level of misalignment should result in a signal from the O-mode cutoff also being observable or would be expected during at least some portion of a plasma shot where the technique is used. Or in the limit of low magnetic fluctuations, measurements would be expected to be below noise levels. Given a single measured peak and the noise level, it is possible to place an upper bound on the contamination level of the cross-polarization signal by density fluctuations within the accuracy of the above approximations.

Using the geometry in figure 1 also prevents spurious scattered light from presenting a problem, which is a critique that has been raised about past cross-polarization scattering experiments. Since the launched beam is refracted, it has no path back through the window after reflections inside the vessel, and spurious reflections should not be a problem. Using a DBS geometry where the localized signal is Doppler shifted also discriminates against spurious signals, which would not be Doppler shifted.

2.2. Wave-vector matching

Momentum conservation for the scattering process dictates selection rules for the wave vector of the scattered wave,

$$\mathbf{k}_s = \mathbf{k}_i + \mathbf{k}_f, \quad (15)$$

where the s , i , f , respectively, are the scattered, incident, and fluctuation waves where the fluctuating quantity could be density or magnetic field. For standard scattering configurations,

the dispersion relation for the wave remains the same, so $|k_i| = |k_s|$. For CP-DBS, this is no longer true. Instead, the scattered wave must fall onto a different dispersion relation for propagation to occur. If we further assume the usual DBS geometry $k_r = 0$ and perfect toroidal alignment $k_{\parallel} = 0$ (where k_r is the radial component and k_{\parallel} is the parallel component of the wave vector), then we have for the binormal component $k_O = k_X + k_f$ at the scattering location, where k_O is the O-mode wave number, k_X is the X-mode wave number, and k_n is the wave number of the scattering density fluctuation. With the change in direction, we have $|k_f| = |k_O| + |k_X|$. One would then expect a slightly different path out of the plasma. For a spherical tokamak, where k_O and k_X 's are not hugely different, this matters less than for a standard tokamak. This effect might, however, limit measurements to near the edge (i.e., a short path length in the plasma, so reduced possibilities for different paths). The factors that determine whether measurements can be made with this technique are therefore the size of the beam (how different the paths can be) and the difference between the dispersion relations and the plasma path length (how different the path is). This can, in principle, be determined via ray tracing or beam tracing techniques. The measurements presented below are localized at the top of the pedestal with at most a few centimeters propagation through plasma, resulting in little possibility for differences in paths to be a significant effect compared to the beam diameter of about 8–10 cm.

2.3. Non-WKB effects

An issue to be considered is non-WKB effects related to polarization interaction in steep density gradients. The discussion above assumes a WKB or geometrical optics approach is valid and that the O-mode and X-mode can be treated as independent modes of propagation with negligible interaction. It is possible for interaction between the characteristic waves when there is large magnetic shear or the density gradient is large [33–35]. This effect is significant when the difference between the O-mode and the X-mode wave numbers is small, $|k_O - k_X| \ll 2\pi/L$, where L is the plasma inhomogeneity length scale. Due to the low magnetic field in a spherical tokamak, the left-hand side can be small. Although there can be large global magnetic shear for the typical measurement region with DBS, on the low field side of the tokamak, the dominant local inhomogeneity affecting microwave propagation is due to the density profile in the H-mode pedestal. In the H-mode pedestal, the density gradient scale length can be on the order of 1 cm. However, in the region where scattering is localized for DBS, either k_O or k_X should be small due to approaching either one of the cutoff surfaces or the other, depending on the launch polarization. Therefore, at least for the region where the scattering is localized, the criterion for significant interaction will rarely be satisfied. The exception would be when the H-mode pedestal height is large enough to contain both cutoffs in which case the interpretation of measurements becomes more complicated. For measurements localized in the core of an H-mode plasma $|k_O - k_X| \ll 2\pi/L$ could be satisfied when the beam propagates through the

pedestal. The result of polarization interaction somewhere along the beam path, but not in the DBS localization region near cutoff, should be indistinguishable from misalignment between the launched polarization and the magnetic field pitch angle at the edge, which can result in detected Doppler shifts from both the X-mode and the O-mode cutoffs. It is important to note that, if the criterion $|k_O - k_X| \ll 2\pi/L$ is true, the polarization interaction could be important even if the launched polarization is perfectly matched and the effects discussed in section 2.1 are completely negligible.

For the CP-DBS, results below the launched waves were 55–75 GHz with X-mode polarization, and the scattering wave numbers were in the range of 5–7 cm⁻¹. The density in the pedestal was not large enough to also localize the O-mode cutoff, so scattering from waves launched with O-mode polarization would come from the core. In the region of the pedestal, the wave number for a wave propagating with O-mode polarization would have been typically 2.0–2.5 times higher than the X-mode wave, so although the criterion might in some cases be marginal, the inequality was not satisfied, and contamination of CP-DBS by density fluctuations should not be an issue. For the cases with standard DBS measurements of density fluctuations, the pedestal density was higher; high enough to localize the O-mode for the lower frequencies, and the inequality was actually satisfied, but due to the large relative difference between the relative density and the magnetic field fluctuation levels, contamination of standard DBS data by magnetic field fluctuations should not be a problem. Prospective future applications of the CP-DBS technique do motivate a more detailed understanding of the issue, in particular, of how much the polarization interaction matters for the scattering processes of interest.

2.4. Purposeful polarization misalignment

To test the expectations from section 2.1, the rotatable polarizer was purposefully set to launch a linearly polarized wave about 10° away from matching to X-mode polarization at the plasma edge during the current flat top. The detailed laboratory measurements of the polarizer in [24] show excellent transmission and reflection properties so that polarization contamination is known to be due to misalignment and not unwanted transmission. Figure 2 shows the result. This shot is also an example of particularly poor radial localization due to scattering misalignment after 170 ms where the Doppler peaks are initially not well defined. In this shot, the plasma current flat top is reached at about 180 ms. At about 220 ms, there are two distinct Doppler-shifted peaks, which are annotated in the figure. The density profiles are consistent with these separately arising from the X-mode and O-mode cutoffs, which implies that the signal from the X-mode cutoff contains significant fluctuation power due to both density and magnetic field fluctuations. This example also shows that, although to verify good polarization matching, it is *necessary* for there to clearly only be a single peak, it is not a *sufficient* condition. This is because all of the scattering alignment considerations discussed in [24] affect the signal from each cutoff independently and the density profile needs to be such that

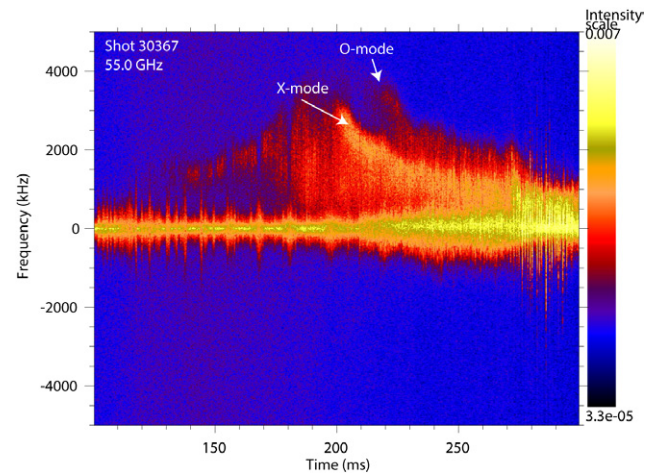


Figure 2. Spectrogram with a logarithmic scale of the DBS data in the cross-polarization configuration with the polarization angle match purposefully misaligned by about 10°, showing the presence of two distinct Doppler-shifted peaks.

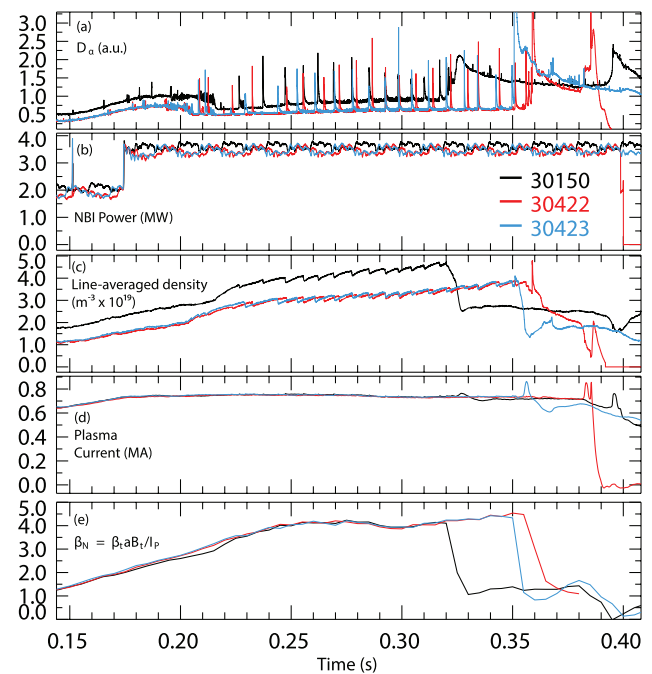


Figure 3. Time traces of (a) D_α emission, (b) NBI power, (c) line-averaged density measured with an interferometer, (d) plasma current, and (e) global β_N .

a signal from both cutoffs would be expected. Therefore, the polarization match also should be assessed independently by comparing the polarizer setting to the magnetic equilibrium reconstruction; however, if the polarization match is poor, it is likely that, at some point within the shot, the O-mode peak should be observed.

3. Experimental results

The plasma conditions simulated in [15], where microtearing was found to be unstable at the top of the pedestal, were attempted to be re-created as a target for using the

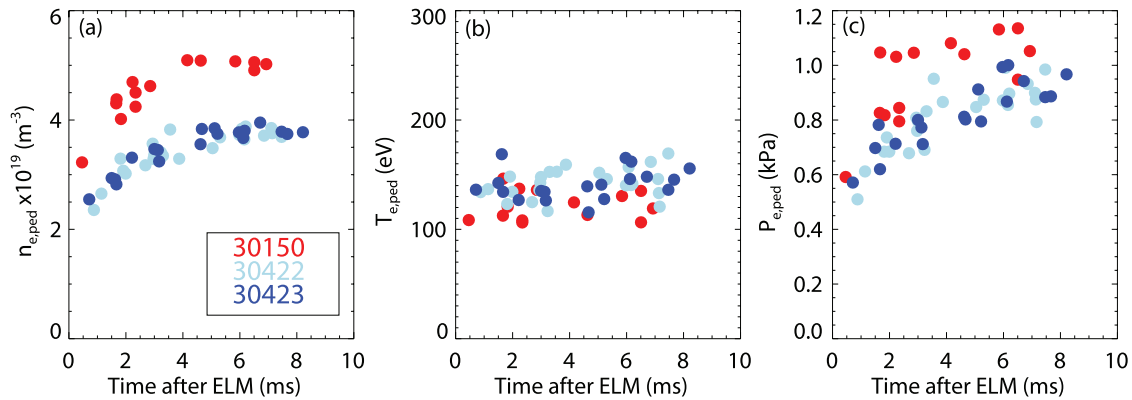


Figure 4. The pedestal height for the (a) density, (b) temperature, and (c) pressure, as a function of time after the preceding ELM, during the steady-state time periods.

cross-polarization Doppler backscattering technique. Similar plasma conditions were realized with the DBS system, both in the standard configuration to measure density fluctuations and in the cross-polarization configuration to measure magnetic field fluctuations. The results are presented in this section.

3.1. Experimental plasma conditions

One shot for standard and two shots for cross-polarization DBS configurations were successfully acquired with conditions similar to [15]. Figure 3 shows time traces during the H-mode period of edge D_α emission, neutral beam injection (NBI) power, line-averaged density, plasma current, and global β_N for the three shots. Shot 30 150 had standard configuration DBS, and the other two had cross-polarization DBS. The density in 30 150 was $\sim 30\%$ higher, and due to differences in wall conditions, exact repeats were not possible; stability calculations below show only small differences between the two cases. For the pedestal, this resulted in a higher density at the pedestal top in 30 150, but slightly higher temperatures in 30 422 and 30 423, which as the best match that could be achieved. The D_α emission shows the periodic activity, which is identified as due to type-I ELMs. For all three discharges, the plasma current during the flat top is 730 kA, the toroidal magnetic field is $B_t \approx 0.47$ T, the safety factor at the edge is $q_{95} \approx 5.5$, elongation $\kappa \approx 1.7$, upper and lower triangularities $\delta_u = \delta_l \approx 0.5$, $\beta_N \approx 4$, and about 3.5 MW injected neutral beam power.

High spatial and temporal resolution electron temperature and density profiles were measured with a Thomson scattering system [36]. Modified-hyperbolic tangent (mtanh) fits to each Thomson scattering profile were performed to assess the evolution of the edge pedestal using the high field side pedestal for better spatial resolution due to flux expansion. After an increase following the L-H transition, the pedestal height and width at the end of each ELM cycle reached a slowly evolving steady state for the time period of 250–350 ms (somewhat shorter in 30 150). Figure 4 shows the evolution of the fit parameters for pedestal density, temperature, and pressure height as a function of time since the last ELM during the steady-state period. The ELM time was determined by spike detection using edge D_α emission. The

qualitative characteristics are the same in all three discharges: The temperature increases slowly throughout the ELM cycle, and the density at first recovers quickly after the ELM, then increases more slowly after about 2 ms. The pressure also at first increases quickly, then more slowly after 2 ms. Quantitatively, 30 150 had higher density, lower temperature, and overall higher pressure pedestal heights than 30 422/30 423 with the pressure height at the end of the ELM cycle about 20% higher in 30 150. The ELM frequency in 30 150 is also slightly higher than 30 422/30 423. The two shots 30 422 and 30 423 were similar, and data from both shots are combined below, while 30 150 is analyzed separately.

The mtanh fit parameters were partitioned into three equal segments of the ELM cycle and were averaged to generate average gradient profiles. The choice of three bins was made to reduce statistical variation observed when using finer time resolution. The result is plotted in figure 5 against ψ , the normalized poloidal flux. The qualitative changes during the ELM cycle are again the same for the three discharges. The location of the largest gradient in all cases moves inward throughout the inter-ELM period. The peak temperature gradient decreases, while the peak density and pressure gradients increase and the overall pressure pedestal width increases. The peak pressure gradient in 30 150 is higher than the two other shots. These averaged profiles are used below as inputs for both the ray tracing routines used to interpret DBS data and the inputs for linear gyrokinetic stability analysis.

3.2. Fluctuation measurements

This section describes DBS measurements acquired during the steady-state H-mode period of the shots described above: 250–350 ms for 30 422/30 424 and 250–300 ms for 30 150. In shot 30 150, the DBS system was arranged for standard scattering to measure density fluctuations with launch and receive in the O-mode polarization for the frequency range of 55–75 GHz. For shots 30 422/30 423 the system was arranged to launch the X-mode and receive the O-mode for the same frequency range. The same ELM cycle-averaged density profiles described above were used as inputs for ray tracing with the code Genray [37] to determine the scattering wave number

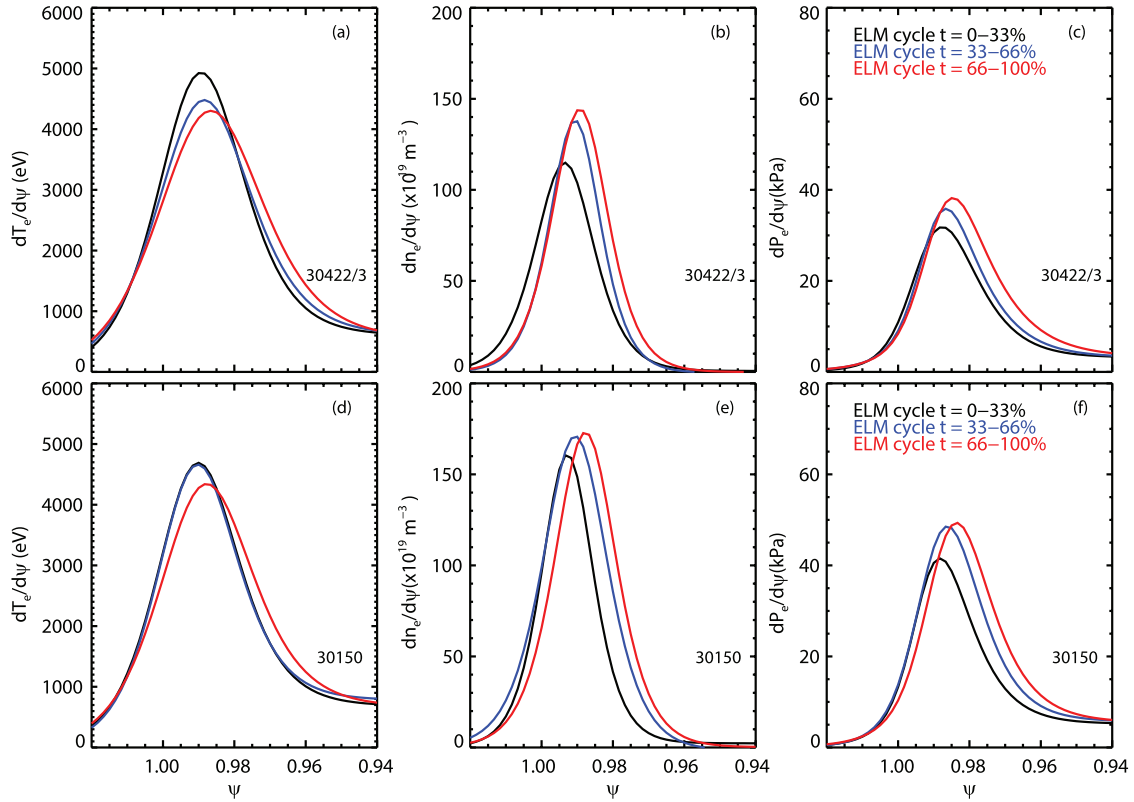


Figure 5. Averaged pedestal temperature [(a) and (d)], density [(b) and (e)], and pressure [(c) and (f)] gradients for shots 30 422/30 423 [(a)–(c)] and 30 150 [(d)–(f)]. Data are from the high field side of the tokamak.

and locations for the measurements with the the last third of the ELM cycle being of most interest.

For shots 30 422/30 423 the rotatable polarizer angle was set to 27° to match (accounting for the polarizer tilt) the approximately 36° magnetic field pitch angle at the edge of the plasma where the DBS beam intersects the last closed flux surface. The polarizer characteristics were described with detail in [24]. After including corrections for the finite toroidal and poloidal launch angles, the launched polarization angle was matched to the plasma magnetic field pitch angle at the edge to less than 1° . Given the uncertainties in equilibrium reconstruction and density profile where precisely it is necessary to match the polarization to the pitch angle (i.e., where the effective vacuum-plasma interface for coupling into the X-mode or the O-mode is located) and other effects, we consider this to be within the uncertainty of a 0° mismatch for the polarization angle. The beam was launched at different poloidal angles in 30 422 and 30 423 to measure different wave numbers and with different toroidal angles to minimize scattering misalignment for each case.

Figure 6 combines the same conditionally averaged Thomson scattering measurements of the pedestal density in figures 4–5 with ray tracing results for scattering locations. The solid lines are the density profiles for 30 422/23, and the dashed lines are the density profiles for 30 150. The symbols on the lines indicate the scattering locations determined by ray tracing using the diagnostic settings for shots 30 422 and 30 150. Early in the ELM cycle, particularly for the CP-DBS measurements, not all of the channels are pedestal localized

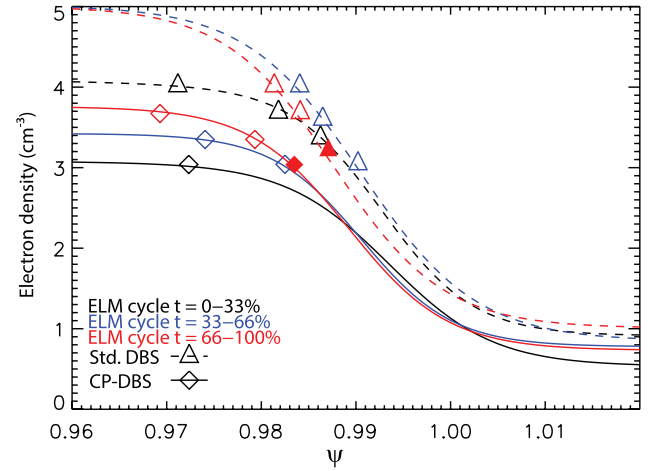


Figure 6. Density profiles and measurement locations during the ELM cycle. The solid (dashed) lines are the conditionally averaged density profiles for 30 422/23 (30 150). The diamonds indicate measurement locations for CP-DBS that were located in the pedestal region, and the triangles indicate measurement locations for standard DBS measurements. The 55 GHz channel location for the last third of the ELM cycle has filled symbols.

with only the lowest frequency localized in the pedestal region for the whole cycle. Note that this indicates that, during some ELMs, even the lowest frequency was core localized at the beginning of the ELM cycle. As the density profile evolves, there is a systematic movement of channels outward in the region of $\psi \approx 0.97$ – 0.99 . For CP-DBS, only the 55 GHz channel is pedestal localized for the first third of the ELM

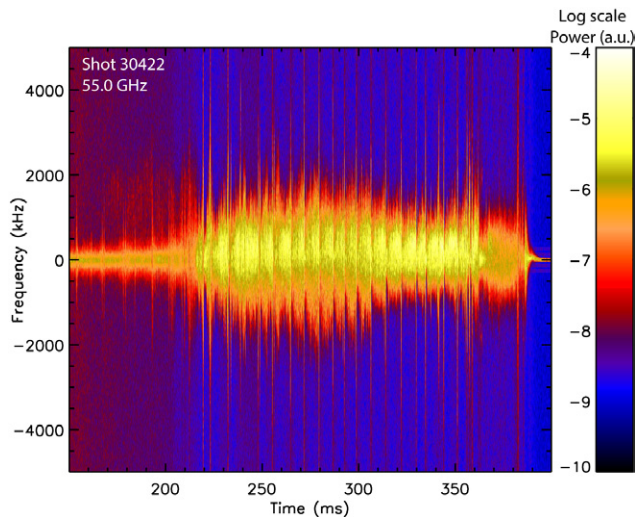


Figure 7. Spectrogram of scattered DBS power in shot 30 422. Beam launched X-mode and O-mode scattering detected. The scale on the right indicates exponents of logarithmic color scale power.

cycle, then two channels for the second third, and three for the last third. For standard DBS, three channels are pedestal localized for the first third, and four are pedestal localized for the last two thirds (only the first three are plotted since data from the fourth are not used later). These conditionally averaged profiles are much more coarse in time resolution than the DBS and CP-DBS measurements, but this does provide information about the evolution of the measurement locations during the ELM cycle. The measurements relied on most in later sections are from the 55 GHz channel during the last third of the ELM cycle, which is denoted with filled symbols.

We also assess the mismatch based on the argument presented in section 2.1. Figure 7 shows a spectrogram of cross-polarization DBS data from shot 30 422. Early in the shot, before ~ 150 ms, there is no Doppler-shifted peak due to the scattering alignment effects discussed in [24]. From figure 3(a), the L-H transition occurs at about 205 ms. Between ~ 150 and 200 ms, there is a very weak signal at ~ 1.5 MHz from the core. After the L-H transition and subsequent rise in density, a strong signal is received from the pedestal region. There is a symmetric signal around zero frequency, which is believed to be from spurious unlocalized scattering along the beam path. During the H-mode period, this overlaps with a Doppler-shifted peak at positive frequency. Gaussian fits to the asymmetric part of the spectrum are performed as described in [24] to quantify the Doppler peak's frequency and amplitude. A broadband burst of power is observed at each ELM, which is not included in the fits. The plasma transitions back to the L-mode and drops in density at about 360 ms due to a large MHD mode. At no point is a second peak observed in the power spectrum as in figure 2, which would be expected at some point if the polarization was not well matched since the O-mode cutoff should be in the core at a position with larger rotation. We cannot rule out a mismatch resulting in scattered power less than the noise level. The signal-to-noise level between the maximum Doppler peak during the H-mode period and the

flat background is about 150 (power ratio; not amplitude). Note this signal level is more than two orders of magnitude less in power than the standard configuration DBS in 30 150. Following from the discussion in section 2.1, we can estimate the bound $R_1 > 150$, which should be equivalent to less than 1% of the received power being due to contamination from the unwanted polarization. From this, the discussion in the previous paragraph, and the previous discussion of non-WKB effects, we proceed with the interpretation that the data in shots 30 422/30 423 are dominated by the cross-polarization signal and are due to local magnetic field fluctuations.

Ray tracing and the ELM-cycle-averaged density profiles were used to determine the scattering locations and wave numbers. For 30 422, three channels (55.0, 57.5, and 60.0 GHz), returned signals from the pedestal with $\psi \approx [0.984, 0.979, 0.970]$ at scattering wave numbers $[5.6, 5.7, 5.9] \text{ cm}^{-1}$ using the ELM-averaged profiles for the last third of the ELM cycle. These locations are near the top of the pedestal. Higher frequency channels were localized in the core, according to both ray tracing and DBS data; the latter exhibited lower amplitude and higher Doppler-shift observations, like the L-mode period 150–200 ms in figure 7. In 30 423, the locations were similar $\psi \approx [0.986, 0.982, 0.978]$, but the wave numbers were higher at $[8.5, 8.8, 9.2] \text{ cm}^{-1}$, respectively. The local ion gyroradius at this location is about 0.5 cm. The difference in physical location between the highest and lowest frequency of the three is also about 0.5 cm, which is of the same order as the radial resolution of the individual channels. The same three channels in 30 150 were located at $\psi \approx [0.987, 0.984, 0.982]$ at wave numbers $[7.0, 7.3, 7.6] \text{ cm}^{-1}$. In all shots under consideration, the same three fixed-frequency channels were located at similar radii with the wavenumbers in standard DBS configuration bracketed by the measurements in the cross-polarization configuration. The scattering alignment mismatch angle (see [24] for details) was $|\theta_{\text{mis}}| \approx 4^\circ$ to 5° and, for a particular frequency and time, was matched to within 1° across the three shots. This means that there is a slight decrease in received power due to the misalignment but that it does not vary between the shots of interest so it does not impact any comparisons of relative fluctuation levels.

In previous work, magnetic probes have been used to identify microtearing modes in the core of RFX-mod [38]. MAST has a number of high frequency Mirnov coils that are digitized at 10 MHz, the same rate as the DBS measurements. Figure 8 shows a spectrogram of one of the fast pick-up coils and the edge D_α for reference where the ELMs correspond to bursts in both D_α and magnetics data. As is typical of a high performance spherical tokamak plasma, there are numerous coherent Alfvénic and MHD modes. At tens of kilohertz, there is a saturated internal kink and its harmonics, which are nearly ubiquitous in MAST plasmas [39]. The modes at 1–1.5 MHz are compressional Alfvén eigenmodes [40]. There is also a variety of activity in the hundreds of kilohertz range—the frequency range where one would expect both ion-scale turbulence and shear Alfvén waves like toroidal Alfvén eigenmodes—including what could be broadband activity related to turbulence during the time period of 200–350 ms, which would be of interest here.

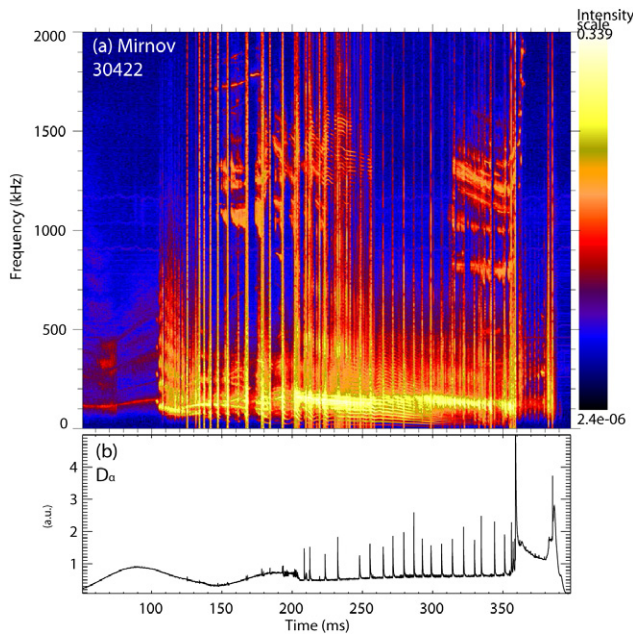


Figure 8. (a) Spectrogram of magnetic pick-up coil on a logarithmic scale and (b) edge D_α emission for reference from shot 30 422.

Cross-correlation analysis between the Mirnov and the DBS data was performed for the three shots under consideration where the ensemble-averaged coherence was calculated for time windows in the H-mode. No significant coherence was found between the Mirnov data and the DBS or CP-DBS signals related to the received scattered power, either the complex scattered electric field or its modulus. Since the DBS and CP-DBS measurements were at $k_\perp \sim 5\text{--}10\text{ cm}^{-1}$, which would correspond to a toroidal mode number in the range of $n \sim 300\text{--}600$, this is not surprising as the magnetic perturbation at those scales would be expected to fall off very quickly in space. For correlations between the Mirnov data and the DBS and CP-DBS phase or phase derivative signals, there is significant coherence for some of the low frequency coherent modes with the largest coherence for the first two harmonics of the saturated kink. This likely appears in the DBS and CP-DBS phase data due to reflectometry-like movements of the cutoff surface and global influence of the ideal kink mode. However, relevant to this paper, we find no significant broadband coherence between magnetic coils and either DBS or CP-DBS data, quite possibly due to being sensitive to different spatial scales.

Figure 9 compares the scattered power between the standard DBS configuration shot and the cross-polarization DBS shots. Referring to figure 3, the large variations in scattered power with time are due to the ELM cycle. There is a qualitative difference where the standard DBS measurements recover rapidly after the ELM then saturate while the CP-DBSs more often monotonically increase through the ELM cycle. This is notably similar to the behavior in figure 4 where the density quickly recovers but the temperature (and overall pressure and β) increase throughout the ELM cycle. The change in the density profile during the first third of the ELM cycle does affect the measurement location, so the observation that the CP-DBS measurements continue to increase during the time period the

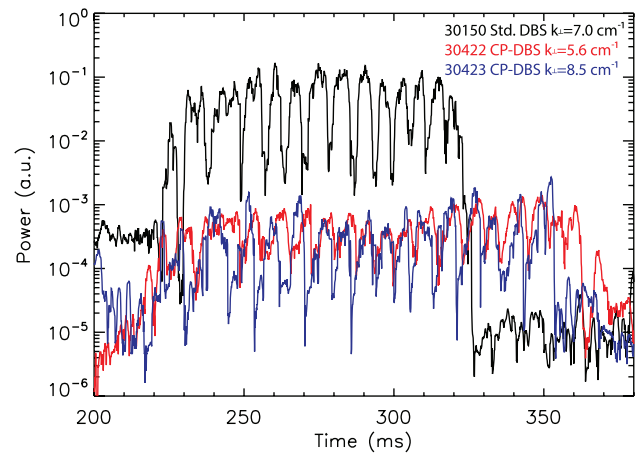


Figure 9. Scattered power comparing the same 55.0 GHz channel in shot 30 150 in the standard DBS configuration and 30 422/30 423 with cross-polarization DBS data.

DBS measurements saturate is more meaningful than differences directly following an ELM. The qualitative differences in the signal do provide further evidence that different fields are being measured. The same 55.0 GHz channel is used for this comparison, so the launched power is the same for all three cases. To implement the hardware arrangement for CP-DBS, changes occurred that would affect the received power. In the standard configuration, a 3 dB directional coupler was used to make the system monostatic. CP-DBS measurements were necessarily bistatic, so the 3 dB coupler was removed, which increased the received power by a factor of 4, all else being the same. The V-band scalar horn antenna used in the monostatic configuration was used for the launch antenna in CP-DBS, and a lower directivity rectangular horn was used for the reception (this also impacted the stray radiation around zero frequency, causing it to be broader), which could marginally increase the received power. Differences in lengths of the waveguide were small and would not be expected to affect signal level. Overall, the hardware changes would be expected to increase the CP-DBS signal power by at least a factor of 4 compared to the standard DBS configuration. Although measuring different wave numbers, the measurements from both CP-DBS shots in figure 9 were of similar amplitude, the simplest implication being a flat fluctuation wave number spectrum over this range (which would also be consistent with active instabilities at those wave numbers); we can then assume these measurements are comparable to the DBS measurements in 30 150 since the wave numbers there were bracketed by 30 422/30 423. There is about a two order of magnitude difference between the DBS and the CP-DBS measurements, which is consistent with the expectation that magnetic field fluctuations should be much smaller than density fluctuations. Although the local gradients for the measurements are slightly different, as seen in figure 6, the approximately two order of magnitude difference is also observed when comparing other channels, discussed further below, which shows the slight difference in local gradients does not strongly impact this result. This is further substantiated in section 4 where it is found that there are only marginal differences in growth rates between

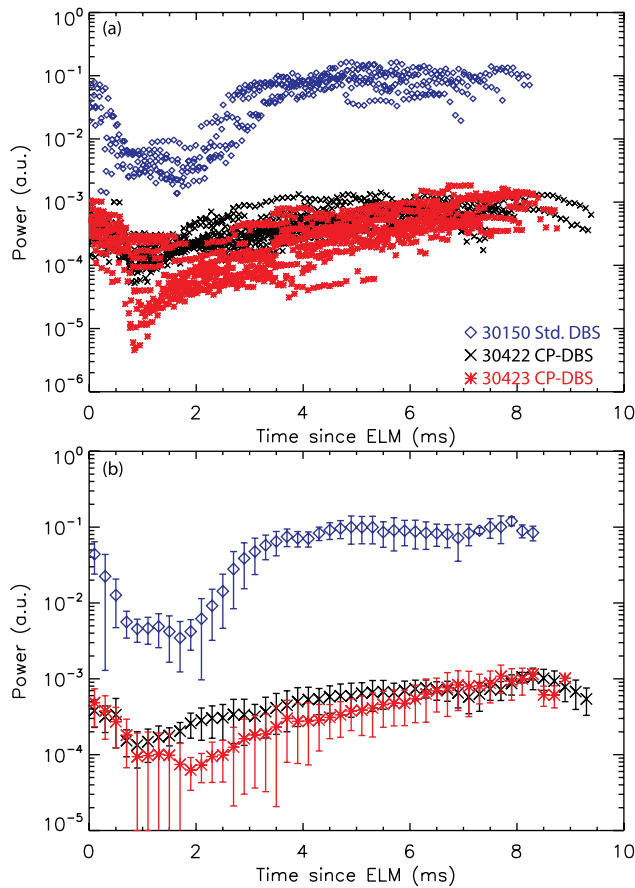


Figure 10. DBS and CP-DBS data plotted against time since the previous ELM: (a) all data and (b) average and standard deviation of data every 200 μ s. All data from the 55.0 GHz channel only.

the DBS and the CP-DBS cases, despite the difference in line-averaged density. Combined with the hardware differences, we then estimate that the relative fluctuation level is about $(\delta B/B)/(\delta n/n) \approx 1/20$.

Figure 10 shows the DBS and CP-DBS data plotted against the time since the previous ELM using the same timing data as in figure 4. The timing was determined using spike detection of D_α emission. Figure 10(a) shows all of the data and (b) bins the data every 200 μ s for the ELM-averaged result where the average is plotted with the standard deviation as the error bar. Data from the same channel, 55.0 GHz, is used here, so the launch power should be the same. There are several notable observations in the plots. First, for both the DBS and the CP-DBS data, the scattered power goes down over the first 0.5–1.0 ms after the ELM—not immediately. The density fluctuations in 30 150 then remain approximately constant between 1 and 2 ms, sharply rise between 2 and 3 ms, then saturate for the rest of the inter-ELM period. Higher levels of scattered power were often measured in L-mode MAST plasmas, so the saturation is unlikely to be due to encountering the nonlinear scattering regime for DBS [41]. Although there is significant variation in the CP-DBS data, the magnetic field fluctuations generally follow a secular rise throughout the inter-ELM period with perhaps saturation for the last 2 to 3 ms, more so for the lower wave number measurement in 30 422.

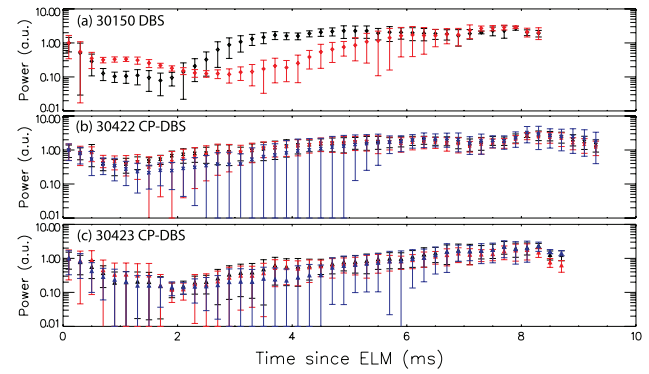


Figure 11. Multichannel DBS and CP-DBS data plotted against time since the previous ELM, normalized for each channel separately for shots (a) 30 150, (b) 30 422, and (c) 30 423. Here black is the outermost channel 55.0 GHz, red is 57.5 GHz, and blue is 60.0 GHz for all three panels.

Comparing the fluctuation measurements in figure 10 to the profile evolution in figure 4, we see that the fast recovery of the density profile is arrested at about 2 ms after the ELM, which is the same time a large increase in density fluctuations in the pedestal is observed. This correlation suggests the increased density fluctuations at wave numbers significantly higher than KBMs (the largest KBM growth rates were about $k_\perp \approx 0.2 \text{ cm}^{-1}$) are related to the evolution of the density profile in the pedestal. At the same time, the secular rise of the magnetic field fluctuations more closely follows the similar secular rise of the temperature pedestal. In figure 5, the peak temperature gradient actually decreases, while the magnetic field fluctuations increase. This implies the magnitude of the magnetic field fluctuations is not driven by the temperature gradient. The increase in local β from the increasing overall pressure would generally be expected to result in larger magnetic field fluctuations and would be consistent with past cross-polarization scattering experiments [27].

Figure 11 shows data from multiple channels that were localized near the top of the pedestal. The data are normalized for each channel to the value at the beginning of the cycle for ease of comparison. The differences between channels, within a particular shot, without normalization is of similar magnitude to the uncertainty in the cross-channel calibration and is not significant. For all panels, data from the 55.0 GHz channel are plotted in black, data from the 57.5 GHz channel are plotted in red, and data from the 60.0 GHz channel are plotted blue (except for omitting 60.0 GHz from the first panel). Higher frequency channels are omitted due to localization in the core for at least some inter-ELM periods, which is clear from the data due to much higher Doppler shifts ($\sim 500 \text{ kHz}$ for the data shown, while some times with Doppler shifts $> 1 \text{ MHz}$ occur for omitted channels). The much higher Doppler shifts from the core occur from jumps in measurement location due to local minima in the density profile inside of the pedestal for some time. This behavior is not clear from figure 6 alone since the profiles are averaged there and only the edge profiles are shown.

The cross-polarization measurements show remarkably little difference between channels where after normalization

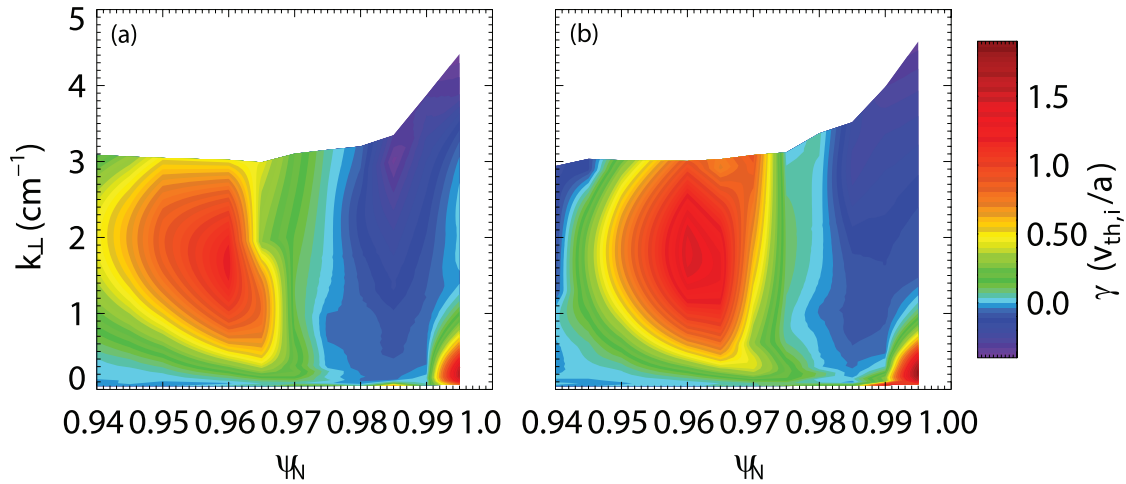


Figure 12. Linear growth rates for (a) 30 150 and (b) 30 422/30 423 for the last third of the ELM cycle at low wave numbers. Growth rate peaks at $k_{\perp} \approx 2 \text{ cm}^{-1}$ are MTMs, and modes at lower- k , to the bottom right of both panels, are KBMs.

there is essentially no difference larger than the plotted error bars for the inter-ELM evolution of magnetic field fluctuations in figures 11(b)–(c). This implies little difference in the behavior of the magnetic field fluctuations at different wave numbers and slightly different radii. In contrast, there is a clear difference between the two DBS channels measuring density fluctuations. They both show a fast rise, then saturation during the ELM cycle but with a delay of $\sim 2 \text{ ms}$ for the inner channel. This implies a difference in either wave number or radius for the turbulence (more likely the radius due to the small difference in wave numbers), which will be compared to linear growth rate calculations in the next section. The difference between the DBS and the CP-DBS channels is again further evidence that different fluctuating fields are being measured.

4. Linear gyrokinetic analysis

Similar to the procedure followed in [14, 15], equilibrium reconstructions were performed with the code HELENA [42] using the conditionally averaged Thomson scattering profiles. The pedestal bootstrap current in HELENA is self-consistently calculated using formulas from Sauter *et al* [43]. For the pedestal region, it was assumed that $T_e = T_i$, which is reasonable for the high collisionality edge (the plasma shape used had a large outer radius that only allowed charge exchange recombination spectroscopy measurements for $\sqrt{\psi} \lesssim 0.85$ and at the outermost measurements $T_e = T_i$ within uncertainties). Since HELENA does not separately account for the fast ion pressure, the central temperatures were increased to match the global poloidal β , β_p , inferred from magnetics measurements. This should reproduce the experimental Shafranov shift. The HELENA results were then used to generate inputs for the gyrokinetic code GS2 [19, 44]. Linear gyrokinetic stability calculations were performed for multiple radii using the equilibrium for the last third of the ELM cycle in shots 30 150 and 30 422/30 423. The electromagnetic calculations were run with 128 points per 2π parallel grid points, a velocity grid

with 16 energy and 72 pitch angle points, two kinetic species (deuterium and electrons), and collisions. Figure 12 shows the resulting growth rates of the fastest growing mode as a function of radius and wave number. Note that, in this plot, the growth rates are normalized to the local value of $v_{th,i}/a$ (where $v_{th,i}$ is the ion thermal velocity and a is the minor radius) and are plotted against the physical k_{\perp} that corresponds to the measured binormal DBS wave number (not the simulation parameter k_y as in [14], which differs by a factor of ~ 2 to 3; the toroidal mode number for the peak growth rate is about the same here as in [14]). Although there were differences in density between 30 150 and 30 422/30 423, the calculated growth rates are generally similar, which validates the comparison of data between the two scenarios.

The plots in figure 12 are similar to the results in [15]. The fastest growing mode at radii $\psi_n \approx 0.98$ – 1.0 is a long wavelength mode with twisting parity, which is identified as the KBM. The HELENA equilibria were also linearly unstable to infinite- n ballooning modes for both cases, which is often used as a proxy for KBM stability. At different radii, these modes propagate in either the electron or the ion diamagnetic direction, which indicates they may be similar to the coupled KBM-trapped electron modes discussed in [45]—an ideal KBM propagates in the ion diamagnetic direction, but coupling to trapped electron effects can result in a mode that propagates in the electron diamagnetic direction. The higher wave number modes at inner radii have tearing parity and are identified as the same microtearing modes discussed in [14]. At a higher wave number and with twisting parity, but at the same radii, figure 13 shows electron temperature gradient modes unstable as well. Both the MTM and the ETG modes propagate in the electron diamagnetic direction. These higher wave number modes were not investigated in [15]. As the MTM and ETG co-exist at the same radii and there is a relatively smooth transition from the MTM as the fastest growing linear mode at lower wave numbers to the ETG at higher wave numbers, this requires careful consideration for interpretation of the measurements with respect to specific instabilities. The DBS and CP-DBS measurements were at wave numbers where the

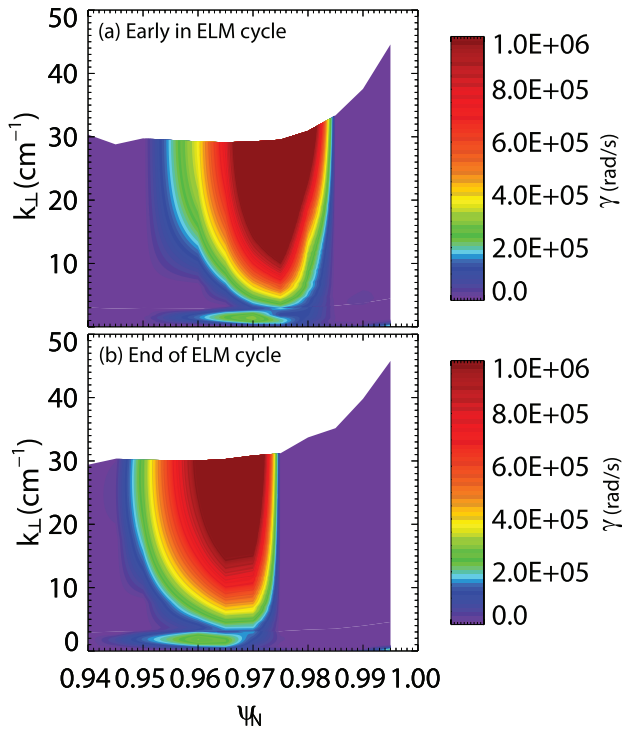


Figure 13. Linear growth rates for 30 422/30 423 comparing times periods (a) close to the start of the ELM cycle and (b) at the end. Growth rate peaks at $k_{\perp} \approx 2 \text{ cm}^{-1}$ are MTMs, modes at higher- k are ETGs, and modes at the bottom right of both panels are KBMs.

ETG was calculated to be the fastest growing mode. However, there is a finite wave number sensitivity for the measurements where with the MAST quasi-optical system [24], we estimate a Gaussian weighting with $\Delta k_{\perp} \approx 2\text{--}3 \text{ cm}^{-1}$ centered at the k_{\perp} determined with ray tracing. With this taken into account, there is a possible overlap between the lower- k CP-DBS measurements and the wave number region where the MTM is the fastest growing mode. These initial value calculations also find only the fastest growing mode, while the MTM could be unstable, but subdominant, where the ETG is fastest growing. To address this, below we consider differences in the linear mode properties.

Figure 10 shows a minimum in the density fluctuation level between 0.5 and 2.0 ms after the start of the ELM cycle. To investigate this, we also constructed equilibria and performed linear GS2 analysis for this time period. Figure 13 compares the growth rates at the beginning (0.5–2.0 ms) and end (last 1/3) of the ELM cycle in 30 422/30 423. Here the growth rates are plotted in dimensional units and are not normalized to local parameters. The most significant change in the MTM and ETG spectra is an inward movement as the pedestal top moves inward, consistent with stabilization of the ETG and MTM in the steep density gradient region. This is also qualitatively consistent with the difference between the density fluctuation measurements at different radii in figure 11(a), suggesting the large increase in observed density fluctuation level occurs as the MTM and ETG unstable region moves inward. The exact measurement and instability locations do not match quantitatively, but the difference of $\psi \sim 0.01$ is within reasonable uncertainty estimates and similar to the diagnostic spatial

resolution. Nonlinearly, one would also expect some finite radial extent for the modes for which these local linear calculations generate no prediction.

In section 3.2 we arrived at the estimate from experimental measurements that the ratio between fluctuation levels was $(\delta B/B)/(\delta n/n) \approx 1/20$. This is a quantity that can be compared to predictions from the linear gyrokinetic simulations. Figure 14 shows the GS2 results for the linear eigenmode structure along the field line for MTM and ETG modes at $\psi = 0.97$ for the last 1/3 of the ELM cycle in 30 422/30 423 for both the density and the magnetic field components of the modes. The density $\delta n/n$, is calculated from the distribution function (a Boltzmann response is not assumed), and the magnetic field $\delta B_r/B$ is determined from the calculated A_{\parallel} after accounting for normalization factors and using the binormal wave number for the mode. It has been shown in other work that MTMs are often not isotropic on the 2D plane normal to the magnetic field, but this is the simplest assumption to make. Typically in other work, $k_r > k_{\perp}$ for the MTM by a factor of order unity, which would make our calculation an underestimate of $\delta B/B$. The plots are normalized to the maximum of $\delta n/n$, so the ratio between fields in the plots is the closest linear correspondent to the experimental measurement. While the experimental measurements were of k_{\perp} perturbations, the calculation is of $\delta B_r/B$, since for the linear calculations, $k_r = 0$ is the fastest growing mode. We are therefore assuming in making the comparison that the linear characteristics of the fastest growing mode determine the ratio of fluctuation levels and that deviations from 2D isotropy are smaller than differences between the modes being compared. There are currently no 2D intermediate- k , high- k measurements, or nonlinear multiscale gyrokinetic simulations in the pedestal that would allow us to better assess the fidelity of these assumptions. These are strong assumptions as it is currently not known how the turbulent cascade, saturation and suppression mechanisms, or other nonlinear effects could impact this comparison.

The eigenmode structures in figure 14 reflect the expected parity for the MTM and ETG. The MTM is tearing parity (φ odd and A_{\parallel} even), and the ETG is twisting parity (φ even and A_{\parallel} odd). The experimental measurements were centered at about $R = 149.4$ and $Z = -5.3 \text{ cm}$, which roughly corresponds to $\theta \approx 0.1$ in the plots. The beam radius also would be expected to be about 4 to 5 cm with a Gaussian shape. Averaging the ratio of the amplitude of the eigenmodes over the points corresponding to the beam size yields $(\delta B_r/B)/(\delta n/n) \approx 0.38$ for the MTM at $k_{\perp} = 0.5 \text{ cm}^{-1}$ and $(\delta B_r/B)/(\delta n/n) \approx 0.019$ (0.015) for the ETG at $k_{\perp} = 7.0$ (2.7) cm^{-1} . The experimental measurements of $(\delta B/B)/(\delta n/n) \approx 1/20$ at $k_{\perp} \approx 6\text{--}8 \text{ cm}^{-1}$ are only about a factor of 2 different from the linear ETG fluctuation ratio, but the MTM is an order of magnitude larger. Along with the better match for the wave numbers, we therefore conclude that the measurements are more consistent with the ETG than the MTM. We also include the higher wave number ETG result in figure 14(c), which shows a significant electromagnetic component to the ETG, which is surprising as the ETG is often considered to be predominantly an electrostatic mode

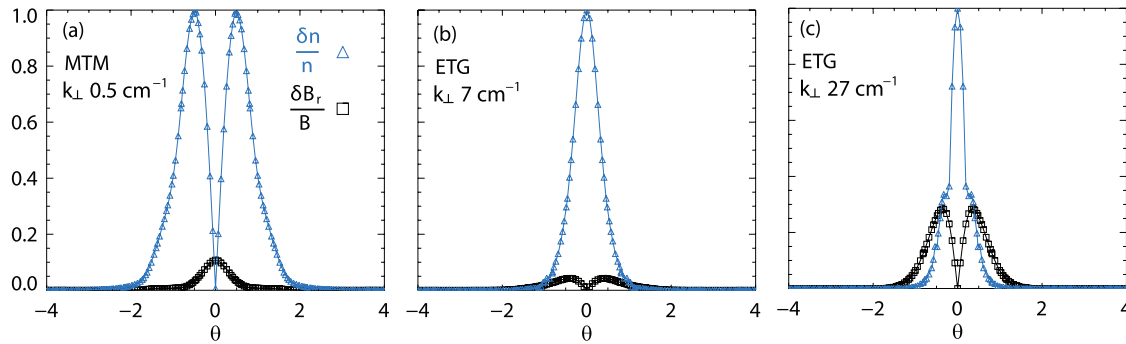


Figure 14. Linear eigenmode structure at $\psi = 0.97$ for (a) MTM at $k_{\perp} = 0.5 \text{ cm}^{-1}$, (b) ETG at $k_{\perp} = 7 \text{ cm}^{-1}$, and ETG at $k_{\perp} = 27 \text{ cm}^{-1}$.

(although simulations first demonstrating that the ETG can drive experimentally relevant levels of heat flux were electromagnetic [19]).

5. Discussion and conclusions

We have presented a description of a novel diagnostic technique, combining DBS and cross-polarization scattering, for the measurement of localized internal magnetic field fluctuations. This is a challenging diagnostic technique, and we have considered a range of effects that can plausibly impact interpretation of cross-polarization measurements. We then used this technique as well as standard DBS in plasma conditions in MAST where we expected microtearing modes to be unstable from previous simulations. Both experimental data and careful assessment of the equilibrium and diagnostic geometry were consistent with successful polarization isolation and negligible impact of other effects so that magnetic field fluctuations were measured. We focused on the evolution of density and magnetic field fluctuations at the top of the pedestal between ELMs. An increase in density fluctuation measurements was correlated with arresting the rapid increase in the density pedestal after an ELM. The measured magnetic field fluctuations showed different behaviors with a secular rise throughout most of the inter-ELM period, consistent with the magnetic field fluctuations being dependent on the local pressure or β . The experimental ratio of fluctuation levels at the end of the ELM cycle was inferred from measurement to be $(\delta B_r/B)/(\delta n/n) \approx 1/20$.

Linear gyrokinetic simulations were performed with the code GS2. We found that both microtearing and electron temperature gradient modes were unstable at the same radii. Electron temperature gradient modes have previously been studied in spherical tokamaks [46–52], including near the top of the pedestal, but are usually thought to be most relevant at much higher wave numbers than we measured here. The measured wave numbers overlapped best with the range of wave numbers where the ETG was the fastest growing mode. The ratio between fluctuation levels in the linear simulations was found to be similar to the experiment for the ETG $(\delta B_r/B)/(\delta n/n) \approx 0.02$ but an order of magnitude larger for the MTM $(\delta B_r/B)/(\delta n/n) \approx 0.4$. Although a number of approximations were made to compare the fluctuation ratios, we estimate they should be at most order unity, which is significantly

smaller than the difference between the MTM and the ETG. The wave numbers and fluctuation ratios are consistent with the ETG explaining the experimental measurements, even though the measured wave numbers $k_{\perp}\rho_i \approx 3$ to 4 are much lower than typically associated with ETG modes (usually thought to be important closer to the electron gyroradius scale $k_{\perp}\rho_e \gtrsim 0.1$, which is closer to $k_{\perp}\rho_i \approx 10$). Given the lower wave numbers, the ETG can be more important for transport than previously thought.

These experimental and simulation results show the ETG is unstable at the top of the pedestal in MAST and suggest that both the ETG and the MTM can be important in the transition region between the steep density gradient in the pedestal and the more shallow gradients in the core. Although the simulations do predict the MTM to be unstable, the measurements do not directly confirm or contradict this prediction due to lack of lower wave number measurements in this study. It is possible that either, both the MTM and the ETG are present, or that the ETG is present, but the MTM is actually nonlinearly stabilized, for instance, via $E \times B$ shear. A fully predictive understanding of the inter-ELM pedestal might then be quite challenging, requiring multiscale physics from peeling-ballooning modes all the way to ETG scales where attempts to modify and control the natural ELM cycle could have differential effects on the various instability mechanisms that affect transport.

Acknowledgments

Thanks to E Gusakov and P B Snyder for useful discussions. This work has been carried out within the framework of the EUROfusion Consortium and has received funding from the Euratom research and training programme 2014–2018 under Grant Agreement No. 633053. This work also received support through the RCUK Energy Programme under Grant no. EP/I501045 and the US Department of Energy under Grant No. DE-FG02-99ER54527. GS2 simulations carried out on HELIOS at IFERC, Aomori, Japan under the Broader Approach Collaboration and ARCHER through EPSRC Grant No. EP/L000237/1. To obtain further information on the data and models underlying this paper, please contact PublicationsManager@ccfe.ac.uk. The views and opinions expressed herein do not necessarily reflect those of the European Commission. JCH's work partly was supported

through the Culham Fusion Research Fellowship and EFDA Fusion Research Fellowship programmes. DD's work was supported by a EUROfusion fusion researcher fellowship (WP14-FRF-CCFE/Dickinson). Dr T Rhodes is gratefully acknowledged for allowing theInspect spectral analysis program to be ported for use with MAST data.

References

- [1] Snyder P B *et al* 2011 *Nucl. Fusion* **51** 103016
- [2] Burckhart A *et al* 2010 *Plasma Phys. Control. Fusion* **52** 105010
- [3] Leyland M J *et al* 2013 *Nucl. Fusion* **53** 083028
- [4] Leonard A W 2014 *Phys. Plasmas* **21** 090501
- [5] Kirk A *et al* 2014 *Nucl. Fusion* **54** 114012
- [6] Solomon W *et al* 2014 *Phys. Rev. Lett.* **113** 135001
- [7] Lloyd B *et al* 2003 *Nucl. Fusion* **43** 1665
- [8] Yan Z *et al* 2011 *Phys. Rev. Lett.* **107** 055004
- [9] Diallo A *et al* 2015 *Phys. Plasmas* **22** 056111
- [10] Diallo A *et al* 2014 *Phys. Rev. Lett.* **112** 115001
- [11] Diallo A *et al* 2015 *Nucl. Fusion* **55** 053003
- [12] Furth H P, Killeen J and Rosenbluth M N 1963 *Phys. Fluids* **6** 459
- [13] Furth H P, Rutherford P H and Selberg H 1973 *Phys. Fluids* **16** 1054
- [14] Dickinson D *et al* 2011 *Plasma Phys. Control. Fusion* **53** 115010
- [15] Dickinson D *et al* 2012 *Phys. Rev. Lett.* **108** 135002
- [16] Saarelma S *et al* 2013 *Nucl. Fusion* **53** 123012
- [17] Manz P *et al* 2014 *Plasma Phys. Control. Fusion* **56** 035010
- [18] Smith D R *et al* 2013 *Phys. Plasmas* **20** 055903
- [19] Dorland W, Jenko F, Kotschenreuther M and Rogers B N 2000 *Phys. Rev. Lett.* **85** 5579
- [20] Jenko F, Told D, Xanthopoulos P, Merz F and Horton L D 2009 *Phys. Plasmas* **16** 055901
- [21] Hatch D R *et al* 2015 *Nucl. Fusion* **55** 063028
- [22] Canik J M *et al* 2013 *Nucl. Fusion* **53** 113016
- [23] Hirsch M *et al* 2001 *Plasma Phys. Control. Fusion* **43** 1641
- [24] Hillesheim J C *et al* 2015 *Nucl. Fusion* **55** 073024
- [25] Lehner T, Rax J M and Zou X L 1989 *Europhys. Lett.* **8** 759
- [26] Vahala L, Vahala G and Bretz N 1992 *Phys. Fluids B* **4** 619
- [27] Zou X L *et al* 1995 *Phys. Rev. Lett.* **75** 1090
- [28] Colas L *et al* 1998 *Nucl. Fusion* **38** 903
- [29] Gurchenko A D *et al* 2005 *Plasma Phys. Rep.* **31** 476
- [30] Rhodes T L, Peebles W A, Crocker N A and Nguyen X 2014 *Rev. Sci. Instrum.* **85** 11D838
- [31] Gusakov E Z and Surkov A V 2004 *Plasma Phys. Control. Fusion* **46** 1143
- [32] Lechte C 2009 *IEEE Trans. Plasma Sci.* **37** 1099
- [33] Ginzburg V L 1961 *Propagation of Electromagnetic Waves in Plasma* (London: Gordon and Breach)
- [34] Budden K G 1952 *Proc. R. Soc. A* **215** 215
- [35] Zheleznyakov V V, Kocharovski V V and Kocharovski V V 1983 *Sov. Phys.—Usp.* **26** 877
- [36] Scannell R *et al* 2010 *Rev. Sci. Instrum.* **81** 10D520
- [37] Smirnov A P and Harvey R W 1995 *Bull. Am. Phys. Soc.* **40** 1837
- [38] Zuin M *et al* 2013 *Phys. Rev. Lett.* **110** 055002
- [39] Chapman I T *et al* 2010 *Nucl. Fusion* **50** 045007
- [40] Sharapov S E *et al* 2014 *Phys. Plasmas* **21** 082501
- [41] Gusakov E Z, Surkov A V and Popov A Y 2005 *Plasma Phys. Control. Fusion* **47** 959
- [42] Huysmans G T A, Goedbloed J P and Kerner W 1991 *Proc. of the CP90 Conf. on Computational Physics* (Singapore: World Scientific) p 371
- [43] Sauter O, Angioni C and Lin-Liu Y R 1999 *Phys. Plasmas* **6** 2834
- [44] Kotschenreuther M, Rewoldt G and Tang W 1995 *Comput. Phys. Commun.* **88** 128
- [45] Guttenfelder W *et al* 2013 *Nucl. Fusion* **53** 093022
- [46] Joiner N *et al* 2006 *Plasma Phys. Control. Fusion* **48** 685
- [47] Mazzucato E *et al* 2008 *Phys. Rev. Lett.* **101** 075001
- [48] Roach C M *et al* 2009 *Plasma Phys. Control. Fusion* **51** 124020
- [49] Smith D R *et al* 2009 *Phys. Rev. Lett.* **102** 225005
- [50] Ren Y *et al* 2011 *Phys. Rev. Lett.* **106** 165005
- [51] Yuh H Y *et al* 2011 *Phys. Rev. Lett.* **106** 055003
- [52] Ren Y *et al* 2012 *Phys. Plasmas* **19** 056125